Enhancing turbulent fluctuation measurement with tailored wind lidar profilers

Maxime Thiébaut [1], Frédéric Delbos [2], and Florent Guinot [1]

[1]France Énergies Marines, Technopôle Brest-Iroise, 525 Avenue Alexis de Rochon, 29280 Plouzané, France
[2]Vaisala France SAS, 6A, rue René Razel, Tech Park, CS 70001, 91400 Saclay Cedex, France

Correspondence: Maxime Thiébaut (maxime.thiebaut@france-energies-marines.org)

Abstract. This study evaluates the impact of an enhanced sampling rate on turbulence measurements using the Vaisala WindCube v2.1 lidar profiler. A prototype configuration, sampling four times faster than the commercial setup, was compared to the commercial WindCube v2.1 with reference measurements provided by a 2D sonic anemometer mounted on a measurement mast. Over the 47-day experiment, the prototype configuration showed performance similar to the commercial setup for key performance indicators (KPIs) like slope and coefficient of determination of mean wind speed compared to reference measurements, with both configurations meeting "best practice" threshold. However, for mean wind speed differences, the commercial configuration met the "best practice" level, while the prototype met the "minimum acceptance" criterion. Additionally, the data availability of the prototype configuration was 0.5% lower than that of the commercial configuration. Moreover, the increased sampling rate in the prototype lidar resulted in higher mean variance in instrumental noise compared to the commercial configuration. Despite this limitation, the mean noise-corrected along-wind variance measured by the prototype lidar was approximately 7% higher than that of the commercial lidar, suggesting that the prototype might be better at capturing additional turbulent energy by resolving smaller eddies. This effect was especially evident at higher wind speeds. Error metrics for the noise-corrected along-wind standard deviation in the prototype lidar were approximately 25% lower than those of the commercial configuration. However, the observed improvements of the prototype configuration in measuring turbulence fell short of expectations due to inherent limitations in the measurement process within the probe, where spatial and temporal filtering effects constrain the detection of turbulence at certain scales.

1 Introduction

Accurate turbulence data enable better understanding and control of wind flow patterns, optimizing the design, operation, and maintenance of wind energy systems. Furthermore, turbulence measurement plays a pivotal role in addressing key challenges within the wind energy sector. It aids in enhancing the efficiency and safety of wind turbine operations, minimizing wear and tear on vital components, and extending the lifespan of these costly assets. Additionally, improved turbulence measurement can facilitate more precise wind resource assessments, aiding in site selection and the overall planning of wind energy projects.

In the wind energy sector, the utilization of wind lidar profiler technology has gained significant traction in recent years, supplanting the traditional meteorological mast equipped with in-situ sensors like cup or sonic anemometers as the standard means of measuring key mean wind properties, such as speed and direction. Wind lidar profilers present compelling advantages, including the potential for cost reduction compared to meteorological masts and the capacity to measure at similar or even greater heights above the ground.

Wind lidars profilers can be categorized according to their emission waveform, i.e., pulsed or continuous, and measuring technique, i.e., Doppler beam swinging (DBS) (Strauch et al., 1984) or velocity-azimuth display (VAD) (Browning and Wexler, 1968). Measurement methods used by wind lidar profilers are fundamentally different from those used by cup or sonic anemometers. Anemometers estimate wind speed over a small volume of just a few cubic centimeters, whereas pulsed lidar profilers provide an average over a cylindrical probe several dozen meters long with a cross-sectional diameter of less than 1 cm (Fig. 1).

However, wind lidar profilers have yet to garner widespread acceptance for turbulence measurement, which remains a focal point of ongoing research. In contrast to turbulence data derived from reference instruments such as sonic anemometers, turbulence data from lidar profiler measurements suffer from systematic errors induced by (i) the inter-beam effect, also known as the cross-contamination effect, (ii) the intra-beam effect, i.e., the averaging effect of the probe volume (Fig. 1) and, (iii), instrumental noise.

The inter-beam effect can result in either underestimation or overestimation of turbulence metrics, arising from the modulation of energy associated with eddies of specific wavenumbers (Kelberlau and Mann, 2020). Any phase difference between the

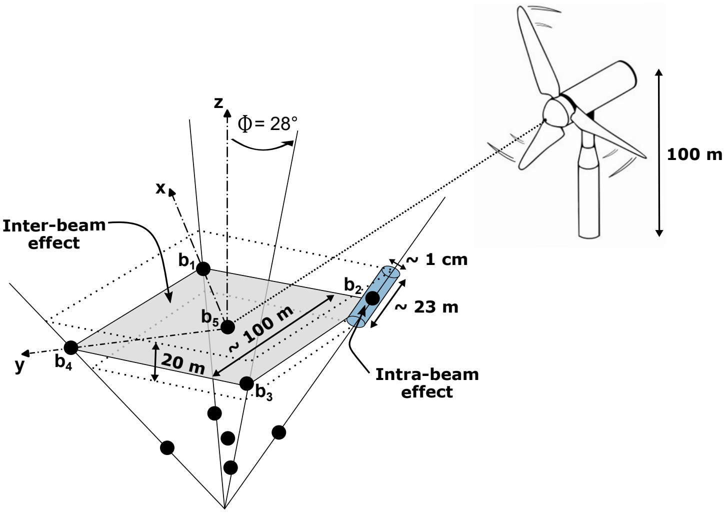

Figure 1. A schematic illustration of inter- and intra-beam effects in the WindCube v2.1 lidar profiler measurement process. The blue cylinder represents the probe volume, corresponding to the dimensions of the commercial lidar configuration. The positions of the five beams are labeled as b_i, where i ranges from 1 to 5. The inclination of the diverging beams (from beam 1 to beam 4) with respect to the vertical z-axis is $\phi = 28^\circ$. Beam 5 is aligned with the z-axis, while beams 1 and 3 are aligned with the x-axis, and beams 2 and 4 are aligned with the y-axis in the coordinate system of the instrument, as stipulated by the manufacturer.

horizontal and vertical components of an eddy significantly impacts the filtering of flow structures, potentially leading to both amplification or attenuation of their measured turbulent energy (Theriault, 1986; Gargett et al., 2009).

The intra-beam effect generates underestimation of turbulence metrics. It arises from two anisotropic filtering processes: (1) spatial filtering due to averaging over the probe volume and (2) temporal filtering caused by averaging over the beam's pulse accumulation time, Δt, at a given measurement position. These two effects give rise to a transfer function, H, applied by the instrument on the signal measured within the probe. The transfer function includes a part due to time-averaging (the sinc term) and a part due to space-averaging (the Gaussian term), such that (e.g., Kristensen et al., 2011):

$$|H|^2(\mathbf{k}) = \mathrm{sinc}^2\left(\frac{\Delta t}{2}\mathbf{k}\cdot\mathbf{U}\right)\exp\left(-\left[\sigma_l^2(\mathbf{k}\cdot\mathbf{b})^2 + \sigma_r^2(\parallel \mathbf{k} \parallel^2 - (\mathbf{k}\cdot\mathbf{b})^2)\right]\right) \tag{1}$$

Here, $\mathbf{k}$ is the turbulent structure wavevector, $\mathbf{b}$ is the beam pointing vector, $\mathbf{U}$ is the vector associated with the wind direction of magnitude U, and σ_l and σ_r represent the Gaussian weighting factors in the along-beam and cross-beam directions, respectively.

From Eq. 1, it follows that wind field structures with wavelengths smaller than σ_l in the along-beam direction are attenuated, as are those with wavelengths smaller than σ_r in the cross-beam direction. However, in the latter case, these structures are so small that the filtering effect becomes negligible, as the cross-section of the probe is approximately 1 cm (Fig. 1). Ultimately, assuming the Taylor frozen turbulence hypothesis, the wavevector domain that passes through the filter is defined by the intersection of two slices: one perpendicular to the direction of $\mathbf{U}$, which preserves structures longer than $\pi\Delta t U$, and another perpendicular to the direction of $\mathbf{b}$, which retains structures longer than σ_l. All other structures are filtered out.

Pulsed lidar profilers require several seconds to complete a full scanning cycle resulting in a low sampling rate that causes discrepancies between turbulence measurements taken by anemometers and those by lidar profilers (e.g., Peña et al., 2009). While the sampling rate governs how quickly the lidar progresses through a scan cycle, it is directly influenced by pulse accumulation time. Consequently, even if the sampling rate is increased, pulse accumulation can still limit the ability of the lidar to resolve small-scale turbulent structures. Since turbulent motion scales vary from milliseconds to hours and from centimeters to kilometers (e.g., Stull, 2000), it is crucial to account for both temporal and spatial filtering effects when assessing lidar-based turbulence measurements.

The concept of measuring turbulence using remote sensing instruments has gradually evolved since the early works in radar meteorology by Lhermitte (1962) and Browning and Wexler (1968). Lhermitte (1969) was the first to propose a method for inferring turbulence by analyzing the variance of radial velocity measurements through VAD scanning. Following this, Wilson (1970) conducted pioneering experiments using a pulsed Doppler radar to detect turbulence within the convective boundary layer (0.1-1.3 km). However, these early measurements were limited to turbulence scales larger than the pulse volume and smaller than the scanning circle, and no validation against reference instruments was performed, questioning their reliability.

Kropfli (1986) expanded Wilson's approach to capture turbulence scales larger than the scanning circle by integrating data from multiple scans. Although initially developed for Doppler radar, these methods were later adapted for Doppler lidar. Eberhard et al. (1989) were the first to apply Wilson's and Kropfli's methods using lidar, and Gal-Chen et al. (1992) further refined the technique with a different scanning configuration. Despite these advancements, the significant probe length (around 100 m) limited studies to the convective boundary layer due to considerable probe volume averaging, especially near the ground. To address this limitation, research shifted towards understanding and mitigating probe volume averaging effects (e.g., Smalikho et al., 2005; Mann et al., 2010; Branlard et al., 2013). Nowadays, modern lidar systems have reduced probe lengths to about 30 m, but averaging effects still pose challenges for turbulence measurements in the surface layer where wind turbines operate (e.g., Mann et al., 2009; Sjöholm et al., 2009; Sathe et al., 2011; Sathe and Mann, 2012).

The present paper delves into the specific advancements pertaining to the Vaisala WindCube v2.1 lidar profiler. A key modification is explored: an augmentation of the sampling rate, achieved by reducing the pulse accumulation time. This customization is evaluated for its impact on the measurement of mean wind speed, data availability, and along-wind variance and standard deviation. The impact of instrumental noise on this modification is also evaluated to demonstrate that the potential improvement in turbulence estimates with the version featuring increased sampling rate is not due to noise.

2 Data and methods

2.1 Prototype configuration with increased sampling rate

The WindCube v2.1 lidar is designed for general atmospheric measurements, such as mean wind speed and direction, requiring a careful balance between temporal resolution, spatial resolution, and carrier-to-noise ratio (CNR). Its default sampling rate is optimized to ensure high data quality and availability across varying altitudes and atmospheric conditions while maintaining system efficiency and manageable data processing.

The WindCube v2.1 employs the Doppler Beam Swinging (DBS) technique to measure wind speed. This method utilizes an optical switch that sequentially directs the lidar beam toward four cardinal directions (0°, 90°, 180°, and 270° from True North), each inclined at $\phi = 28°$ from the vertical. A fifth beam is directed vertically upwards, resulting in wind measurements at five distinct positions (Fig. 1-2).

In its standard commercial configuration, the WindCube lidar collects data at each position for approximately $\Delta t = 0.8$ seconds before switching to the next. Including transition times, a complete DBS scan is performed in 4 seconds, yielding a line-of-sight (LOS) velocity sampling rate of 0.25 Hz. This sampling rate is well-suited for capturing turbulent structures larger than 100 meters. However, wind turbine components experience loads from turbulence across a wide range of scales. Increasing the sampling rate is crucial for broadening the velocity spectrum captured by the lidar, potentially enabling the detection of smaller-scale turbulence that influences turbine performance.

Theoretically, a higher sampling rate improves temporal resolution and extends the resolved turbulence frequency range. However, for wind lidar profiler technology, this enhancement comes with trade-offs. The duty cycle, which represents the proportion of time the lidar transmits pulses, decreases as sampling rate increases, potentially reducing signal strength. Moreover, increasing the sampling rate requires a reduction in accumulation time, resulting in fewer pulses per sample and increasing noise. The default WindCube v2.1 configuration balances these factors to maximize data reliability. It integrates a high number of pulses per measurement to enhance signal quality, making it well-suited for general wind resource assessment. However, its probe length of approximately 23 meters (Fig. 1) limits its ability to resolve small eddies compared to point sensors like sonic anemometers.

In response to the demand for capturing the energy of smaller eddies, we developed a modified version of the WindCube v2.1 that operates four times faster, achieving a LOS velocity sampling rate of 1 Hz. This modification was achieved by reducing the accumulation time for data collection from each beam in conjunction with a reduction in the number of transmitted pulses. The factor of 4 was chosen as a compromise between increasing temporal resolution and maintaining an acceptable CNR and data availability. This choice is intended to keep wind measurements comparable to those from the commercial configuration while enabling the investigation of smaller-scale turbulence. The actual impact on measurement performance will be assessed in the study.

2.2 Field measurement

2.2.1 Measurement site and data collection

The field measurement campaign was carried out by DNV-GL at the lidar validation test site in Janneby, Germany (Fig. 3). Due to its flat terrain, the site features orography-undisturbed flow, which is suitable for the verification trials of lidar systems. The site has relatively good exposure to largely undisturbed wind conditions, i.e., undisturbed winds from almost all sectors. The elevation of the site is a few meters above mean sea level, and the surface roughness is low due to the primarily agricultural land use (Fig. 3a). Two wind turbines (WT N100 and WT N117 in Fig. 3a) are installed in the vicinity of the meteorological

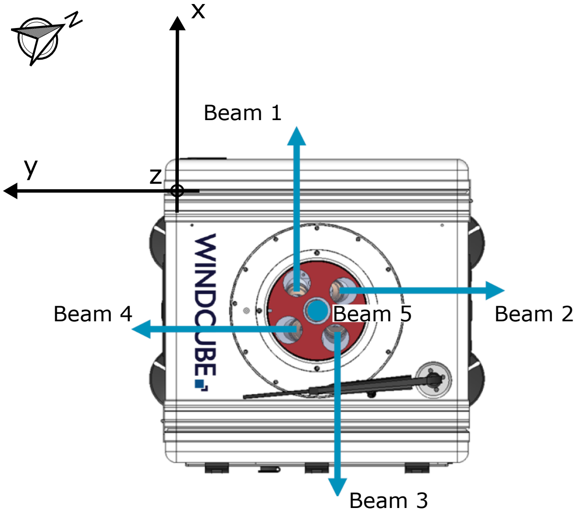

Figure 2. Top view of a WindCube v2.1 lidar showing the positions of its five beams. The x-axis is oriented from beam 3 towards beam 1, the y-axis extends from beam 4 towards beam 2, and the vertical z-axis points upward along beam 5. The arrow indicates North. For the present study, the primary x-axis of the lidars was oriented at -62° relative to North.

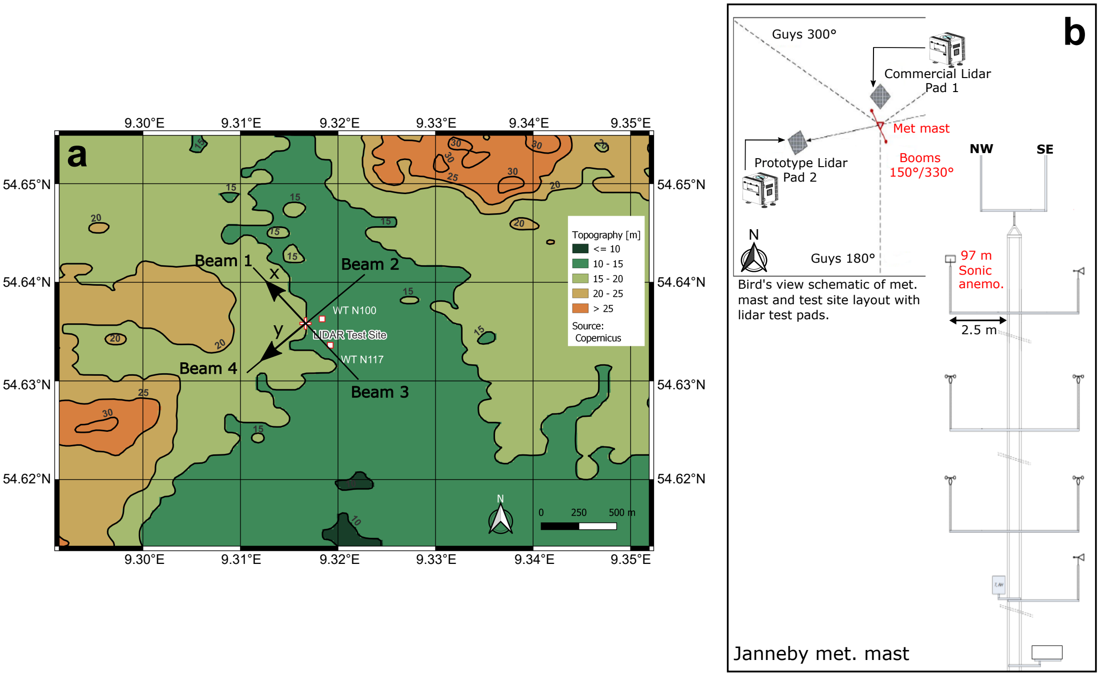

Figure 3. a: Test site location at Janneby, Germany. Black lines indicate the beam orientations for the commercial and prototype configurations. The x and y axes of the instrument coordinate system (see Fig. 2) are marked with black arrows. b: Configuration of the meteorological mast, showing the position of the sonic anemometer. NW and SE denote the north-west and south-east directions. The schematic in panel b also provides a bird's-eye view of the meteorological mast and test site layout, including the lidar test pads.

mast. The closest wind turbine is located 210 m from the mast. A few human constructions (houses, sheds), not exceeding 15 m in height, are located approximately 500 m southwest of the mast.

The meteorological mast is a 100 m, 3-fold guyed lattice tower with a constant face width of 0.4 m. It is equipped with six MEASNET-calibrated Thies First Class Advanced cup anemometers (No. 4.3352) and a Thies 2D sonic anemometer (No. 4.3830). However, only the Thies 2D sonic anemometer is used in this study to provide reference measurements of mean wind speed and turbulence, as the cup anemometers data are not available. The mounting arrangements are consistent with the currently valid IEC and IEA recommendations for the use of anemometry at meteorological masts. As shown in Fig. 3b, the sonic anemometer is pointing towards 150° from True North and is mounted at 97 m above ground, which corresponds to the average hub height of modern land-based wind turbines. The sonic anemometer was set to record continuous horizontal wind speed and direction at sampling rates of 4 Hz.

Adjacent to the measurement mast, both the commercial lidar configuration, and a prototype version with an enhanced sampling rate were installed 3 m and 13 m apart the mast respectively. The prototype configuration was set to record the LOS velocity four times faster than the commercial configuration, as described in Section 2.1. The lidar was aligned such that beams 1 and 3, which correspond to the x-axis (Fig. 2), were oriented at -62° from True North (Fig. 3). According to the manufacturer's recommendation, the x-axis is the primary axis and should be oriented relative to North. Beams 2 and 4 are fixed along the y-axis.

The field measurement campaign was conducted over two periods: from 12 to 25 November 2021, and from 07 December 2021 to 10 January 2022. These two measurement periods were combined to form a 47-day dataset. To facilitate a comparison of turbulence measurements, the sonic-derived wind dataset was resampled to match the sampling rate of the LOS velocities measured by the prototype configuration. This ensures that similar turbulence time scales are captured when calculating and comparing turbulence estimates. Therefore, the sonic anemometer measurements were resampled at 1 Hz.

The 47-day dataset was divided into 2256 subsets of 30-minute data records, with each subset containing 450 and 1800 measurement points for wind data acquired at sampling rates of 0.25 Hz and 1 Hz, respectively. The choice of a 30-minute window deviating from the standard 10-minute window typically used in the wind energy industry was informed by considerations of reduction of random errors in turbulence measurements, as discussed by Lenschow et al. (1994).

2.3 Velocity spectra

Power spectral density of the velocity, i.e., the velocity spectra, provide valuable information about the distribution of turbulent kinetic energy across different scales of motion within the wind flow. This understanding helps in characterizing turbulence and its effects on wind turbine performance and structural loads.

Velocity spectra were computed using Welch's method (Welch, 1967). This method computes an estimate of the spectrum by dividing the data into overlapping segments, computing a modified periodogram for each segment and averaging the periodograms. The Hann window with 50% overlap was applied to each segment to reduce spectral leakage and improve frequency resolution. The 50% overlap is a reasonable trade off between accurately estimating the signal power, while not over counting any of the data.

Following the recommendations of Kelberlau and Mann (2020), turbulence velocity spectra computed from the lidar-derived reconstructed velocity component should not be fitted to turbulence models. This is due to the inter-beam effect, which distorts the spectra, rendering them physically meaningless. Therefore, such spectra were not considered in this study. The focus was on velocity spectra $S_i(f)$ derived from the LOS velocities measured by beam i. The primary limitation in this approach is the intra-beam effect. Spectra were computed for each 30-minute subset of data.

The spectra, $S_i(f)$, were fitted by a parametric expression (Teunissen, 1980; Olesen et al., 1984; Tieleman, 1995) in the frequency domain f, to which we add a component N_i associated with the power spectral density of instrumental noise of the LOS velocity measured by beam i (see section 2.4):

$$S_i(f) = \frac{m}{(1+nf)^{\beta}} + N_i \tag{2}$$

The coefficient m primarily controls the vertical scaling or amplitude of the spectum whereas n influences the rate at which the function decays as f increases. The exponent β determined the shape of the spectrum.

Three different weighting schemes were considered: an unweighted scheme, a low-frequency weighted scheme with weights proportional to the logarithm of the frequency, and a high-frequency weighted scheme with weights inversely proportional to the logarithm of the frequency. Assessing the fitting accuracy included comparing the variance obtained from the integrated fitted spectra with the measured spectra, and calculating their absolute relative differences.

2.4 Instrumental noise

Lidar measurements are inherently influenced by signal noise and potential variations in aerosol fall speeds, both of which contribute additional terms to the observed variance. Assuming that all atmospheric flow contributions to the observed LOS velocity variance within the considered short timescales are of a turbulent nature, the variance $\sigma_{b_i}^2$ of the LOS velocity measured by beam i, can be expressed as the sum of three independent terms (Doviak and Zrnic, 1993):

$$\sigma_{b_i}^2 = \sigma_{p_i}^2 + \sigma_{n_i}^2 + \sigma_{d_i}^2 \tag{3}$$

Here, $\sigma_{p_i}^2$ represents the net contribution from atmospheric turbulence at scales measurable by the lidar (Brugger et al., 2016), $\sigma_{n_i}^2$ denotes the variance associated with instrumental noise, and $\sigma_{d_i}^2$ accounts for the variance caused by variations in aerosol terminal fall speeds within the measurement volume. However, $\sigma_{d_i}^2$ can typically be neglected, as particle fall speeds are generally less than 1 cm/s (e.g., Bodini et al., 2018). Noise will be identified through two different methods: a spectral approach and an autocorrelation approach, as accurately identifying the variance of noise is critical to our study.

2.4.1 Spectral method

Instrumental noise is a critical factor in the spectral analysis of velocity time series. In the spectrum of a velocity time series, this noise typically manifests as a flattening of the spectrum at higher frequencies, indicating a white noise characteristic that contributes equally across these frequencies (e.g., Thomson et al., 2012; Durgesh et al., 2014; Guerra and Thomson, 2017; McMillan and Hay, 2017; Thiébaut et al., 2020). At lower frequencies, the spectrum is usually dominated by the actual signal, which may show a characteristic decay or specific features related to the physical process being measured, such as turbulence. As frequency increases, the influence of the instrumental noise becomes more prominent, leading to a flattened spectral region where the noise dominates.

In Eq. 2, N_i represents the constant power spectral density of noise, which contributes to the spectral flattening observed at higher frequencies. The variance of the noise depends on the technical characteristics of the device measuring the velocity, such as Nyquist velocity, the signal spectral width, the number of pulses and points per range gate, and the signal-to-noise ratio. Theoretical expressions for the variance of this noise can be derived and subsequently removed from the computed turbulence metrics to improve accuracy (Pearson et al., 2009; O'Connor et al., 2010; Bodini et al., 2018, 2019; Wildmann et al., 2019). However, the technical specifications of lidar profilers are no longer openly shared with users, making it impossible to evaluate this noise theoretically. To address this, it is essential to evaluate the noise using an alternative method, such as the spectral approach employed in this study. This approach is comparable to the method proposed by (e.g. Richard et al., 2013; Durgesh et al., 2014). It enables the determination of the power spectral density of noise, N_i, associated with the LOS velocity measured by beam i. Subsequently, the variance of the instrumental noise, $\sigma_{n_i}^2$, can be derived by multiplying N_i by the Nyquist frequency, f_N, such as (e.g., McMillan and Hay, 2017):

$$\sigma^2_{n_i} = N_i f_N \tag{4}$$

2.4.2 Autocorrelation function method

An alternative method for computing the variance of the instrumental noise involves the calculation of the auto-correlation function (ACF) of the squared LOS velocity time series, as proposed by Lenschow et al. (2000). The ACF quantifies the similarity between a signal and its time-shifted versions across various time lags. This measure provides insight into how much of the signal correlates with its past values, which is essential for distinguishing between the noise and signal components.

According to Lenschow et al. (2000), after calculating the ACF, the ACF values (excluding the first lag) are fitted to a $2/3$ power-law function. This power-law model describes the decay of correlation over time, allowing for the extraction of a coefficient that characterizes how the correlation diminishes as the time lag increases. From this power-law fit, the value of the ACF as the lag tends to zero is estimated by extrapolation of the fitted model. This value is associated with the signal variance.

Subsequently, the total variance of the signal is calculated. The instrumental noise variance, $\sigma^2_{n_i}$, is then determined by subtracting the signal variance, as derived from the fitted power-law model, from the total variance. This process enables the separation of the signal and noise contributions to the overall variance. However, this method performs correctly only if the range in which the turbulent cascade occurs is fully captured. This condition is not guaranteed with wind lidar profiler measurements, as the intra-beam effect disturbs the inertial range of turbulence where the cascade takes place.

2.5 Computation of the variance in instrument coordinates

The conventional method for computing variance and standard deviation (the square root of variance) from wind lidar profiler measurements relies on deriving second-order statistics from the reconstructed instantaneous velocity components based on LOS velocities. This approach inherently combines, at each time step, measurements taken at sampling points separated by several tens of meters, depending on the height level of interest. The assumption of instantaneous flow homogeneity (inter-beam effect) introduces an uncertainty in the derived statistics, which is difficult to quantify and can lead to either an overestimation or underestimation of the standard deviation, depending on the frequency and flow configuration. Additionally, this traditional method is affected by both intra-beam filtering and instrumental noise. Crucially, because variance is computed from the reconstructed instantaneous velocity components, it does not account for the noise-induced variance present in the LOS velocity time series which will result in overestimation of variance.

The combined influence of the inter-beam effect, intra-beam effect, and instrumental noise can result in variance estimates derived from the traditional approach that may appear to align more closely with those derived from a sonic anemometer, but for reasons unrelated to the actual turbulence characteristics. Consequently, the benefits of an increased sampling rate for turbulence measurement using a lidar profiler cannot be accurately assessed with this approach.

The variance method, as referred to in the studies (e.g., Stacey et al., 1999a, b; Lu and Lueck, 1999; Rippeth et al., 2002; Guerra and Thomson, 2017; Thiébaut et al., 2022), offers an alternative to the traditional approach for computing variance. This method calculates the second-order statistics of the three velocity components by deriving them directly from the second-order statistics of the LOS velocities. Unlike the traditional approach, the variance method is unaffected by the inter-beam effect. However, it is still influenced by the intra-beam effect and instrumental noise. Notably, the impact of instrumental noise can be identified and removed. Hereafter, a hat notation is used to denote standard deviation or variance derived from this method.

The variance method enables the calculation of the variances, $\hat{\sigma}_x^2$ and $\hat{\sigma}_y^2$ of the velocity components u_x and u_y (in instrument coordinates) as:

$$\hat{\sigma}_x^2 = \frac{1}{2\,\sin^2\phi}\left(\sigma_{p_3}^2 + \sigma_{p_1}^2 - 2\,\cos^2\phi\,\sigma_{p_5}^2\right) \tag{5}$$

$$\hat{\sigma}_y^2 = \frac{1}{2\,\sin^2\phi}\left(\sigma_{p_2}^2 + \sigma_{p_4}^2 - 2\,\cos^2\phi\,\sigma_{p_5}^2\right) \tag{6}$$

where $\sigma_{p_i}^2$ = $\sigma_{b_i}^2$ - $\sigma_{n_i}^2$ (Eq. 3), is the variance of the LOS velocity recorded by beam i, corrected for the variance of instrumental noise.

In this paper, we restrict the application of the variance method to situations where the wind aligns with a single pair of opposite beams (either pair 1-3 or pair 2-4) of the lidar profilers. This alignment condition was met in 17.1% of the cases. Under these conditions, it can be reasonably assumed that the covariance term, $\hat{\sigma}_{uv}$ (where v represents the cross-wind velocity), which corresponds to $\hat{\sigma}_{xy}$ in this specific condition, is negligible (e.g., Newman et al., 2016). Specifically, when the wind aligns with beams 1 and 3, we have $\hat{\sigma}_u^2 = \hat{\sigma}_x^2$. Conversely, when the wind aligns with beams 2 and 4, it follows that $\hat{\sigma}_u^2 = \hat{\sigma}_y^2$. For brevity, we use $\hat{\sigma}^2$ in place of $\hat{\sigma}_u^2$ hereafter. The standard deviation, $\hat{\sigma}$, is then compared to the along-wind standard deviation, σ, which is derived from sonic anemometer measurements.

2.6 Key performance indicators and acceptance criteria

The first step of our analysis focuses on key performance indicators (KPIs), applied to mean wind statistics such as wind speed, that are the mean differences, slope, or the coefficient of determination (R^2) at reference heights corresponding to sonic anemometer measurements. DNV-GL has defined acceptance criteria (ACs) as "best practice" and "minimum allowable tolerances" These criteria, applied to wind speed, flag any KPIs outside the thresholds as "deviations". Table 1 summarizes the ACs established by DNV-GL, which are tested in this paper for the wind speed KPI.

Additionally, the paper addresses data availability. Data availability is defined as the ratio of valid data points returned by the lidar to the maximum number of possible points that could be acquired during the test. To pass the test, DNV-GL set the data availability threshold at 90%.

2.7 Error statistics metrics

This paper focuses on turbulence measurements, specifically the standard deviation of wind velocity, obtained from both the commercial and prototype lidars. These measurements are compared to the standard deviation provided by the reference instrument; the sonic anemometer. To assess the accuracy and reliability of the lidar measurements, various error statistics are used. These include Root Mean Square Error (RMSE), which quantifies the average magnitude of errors; Mean Absolute Error (MAE), which calculates the average absolute difference between predicted and observed values; bias, which represents the systematic error between the lidar and reference measurements; the coefficient of determination, R^2, which indicates the proportion of variance in the lidar measurements explained by the reference data; and relative error, which expresses the error as a percentage of the reference measurement. Together, these statistical metrics provide a comprehensive evaluation of the lidar's performance in capturing turbulence characteristics relative to the reference instrument.

3 Results

3.1 Mean wind speed and data availability

The first step in proposing enhancements to lidar technology is to evaluate their impact on mean wind speed measurements. Fig. 4a illustrates that the mean vertical wind speed profiles measured by both configurations are closely aligned. However, the difference between the mean wind speed measurements provided by the commercial configuration and the reference measurement (black cross in Fig. 4) at the reference altitude is smaller, amounting to 0.98%, compared to a 1.41% difference for the prototype configuration. These results demonstrate that the commercial configuration closely matches the "best practice" AC criterion for the difference in mean wind speed, while the prototype configuration, with a larger difference, only meets the "minimum" criterion (Table 1 and Table 2).

Moreover, the commercial configuration exhibits data availability ranging from 99.5% at the lowest measurement height, i.e., 40 m above the ground, to 93.0% at the highest, i.e., 200 m above the ground, with an overall vertical average availability

Table 1. Acceptance criteria for KPI of mean wind speed in wind lidar profiler certification.

KPI - Wind speed	Definition	Best practice	Minimum	Deviation
Difference	Percentage difference in mean wind speeds between lidar and reference over the verification campaign, relative to the campaign mean wind speed.	< 1%	[1-1.5]%	> 1.5%
Slope	Slope from single-variable regression, constrained to pass through the origin.	[0.98 – 1.02]	[0.97 – 1.03]	< 0.97 or > 1.03
R^2	Correlation coefficient from single-variable regression.	> 0.98	> 0.97	$\leq$ 0.97

Table 2. Acceptance criteria for KPI achievement applied on mean wind speed associated with the commercial and prototype configurations: ✓✓denotes "best practice" and ✓indicates "minimum" acceptance, as defined in Table 1.

	Difference	Slope	R^2	Data availability
Commercial configuration	✓✓	✓✓	✓✓	✓✓
Prototype configuration	✓	✓✓	✓✓	✓✓

of 98.2% (Fig. 4b). Similarly, the prototype configuration follows this trend, with data availability decreasing with altitude. The prototype achieves a vertical average availability of 97.7%, with a minimum of 92.3% recorded at the highest measurement altitude. The prototype configuration consistently shows data availability that is, on average, 0.5% lower than the commercial configuration at nearly all measurement altitudes. Both lidar configurations exceed the 90% data availability threshold set by DNV-GL.

Fig. 5 presents the linear regression of the 30-minute averaged wind speed measured by both lidar configurations in comparison to the reference instrument. Both the commercial and prototype configurations match the "best practice" criteria, with slope values of 1.0 and R^2 values of 0.9847 for the commercial configuration. The prototype configuration shows values that are 1% lower for the slope and almost similar R^2, but these differences are minimal and still within the acceptable range for "best practice."

3.2 Impact of sampling rate on turbulence energy capture

The impact of increasing the sampling rate on turbulence measurement can initially be assessed using data from a sonic anemometer, specifically through the computation of along-wind velocity spectra. Integrating these spectra provides the along-wind variance, σ^2. Fig. 6 illustrates the individual spectra and the mean spectrum averaged over the 47-day dataset in both

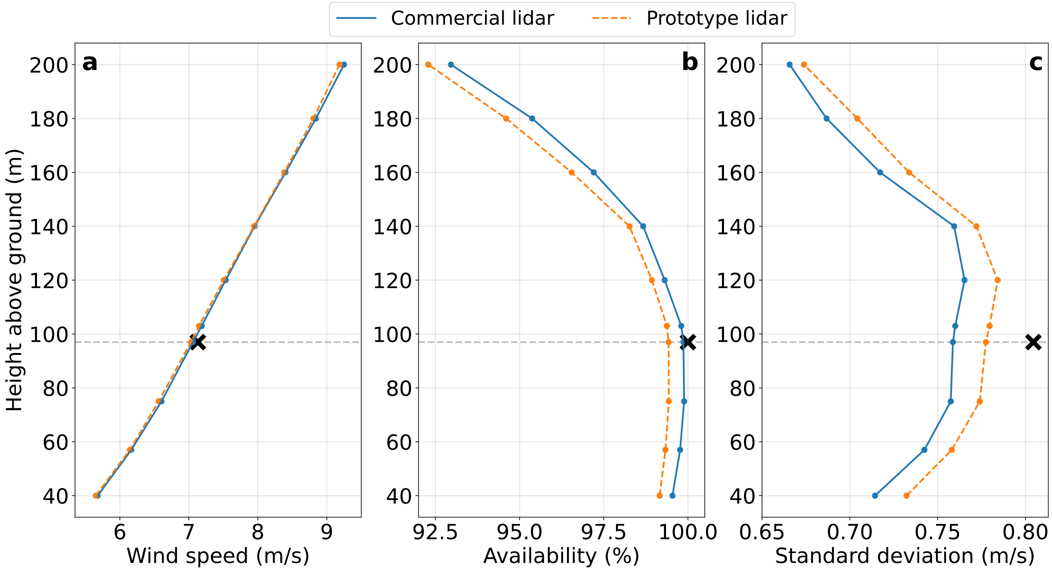

Figure 4. Mean vertical profiles, averaged across the 47-day dataset, of wind speed (a), data availability (b), and standard deviation derived from the variance method (c), measured using the commercial (solid blue curves) and prototype (dashed orange curves) configurations. The black crosses represent the reference measurements from the sonic anemometer, and the grey dashed vertical line marks its position at 97 m above ground.

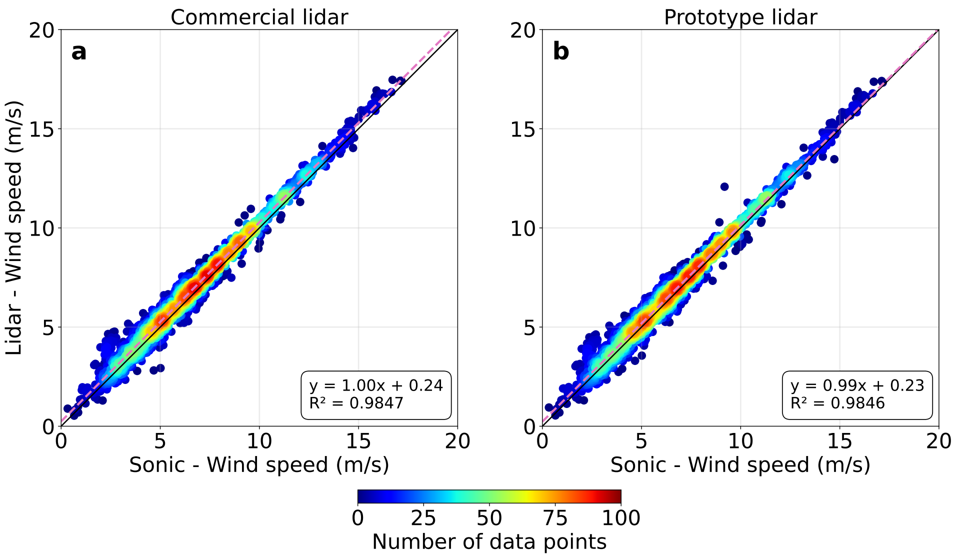

Figure 5. Scatter plots of the 30-minute averaged wind speed measurements over the 47-day campaign, comparing the commercial lidar (a) and prototype lidar (b) with the reference sonic anemometer.

log-log and linear formats. The mean spectrum clearly follows the $f^{-5/3}$ slope, confirming the presence of the energy cascade (Fig. 6a).

The linear representation (Fig. 6b) highlights that most of the energy, associated with larger eddies, is concentrated in the frequency range from 0 to $f_{N_c} = 0.125\,\mathrm{Hz}$, corresponding to the Nyquist frequency of the LOS velocity in the commercial lidar configuration. However, additional energy, associated with smaller eddies, exists within the range from f_{N_c} to $f_{N_p} = 0.5\,\mathrm{Hz}$, the latter being the Nyquist frequency of the prototype lidar configuration.

To quantify this effect, the variance was computed by integrating the spectra over two frequency ranges. First, the integration from 0 to f_{N_c} simulated the variance measurable by a sonic anemometer with a sampling rate equivalent to the commercial lidar. This yielded a mean variance of $0.47\,\mathrm{m}^2/\mathrm{s}^2$. Second, the integration from 0 to f_{N_p} simulated the variance measurable with a sampling rate equivalent to the prototype lidar, resulting in a mean variance of $0.63\,\mathrm{m}^2/\mathrm{s}^2$. This comparison indicates that increasing the sampling rate by a factor of 4, relative to the commercial lidar configuration, could capture an additional 34% of the energy associated with smaller eddies. However, this represents the maximum possible improvement, as it is derived from measurements using a sonic anemometer, which is not affected by technical limitations such as the probe length of a wind lidar profiler.

3.3 LOS velocity spectra

The determination of the instrumental noise from the spectral method involves computational fitting of the LOS velocity spectra using a parametric expression (Eq. 2). Three weighting schemes were systematically explored to enhance fitting accuracy and

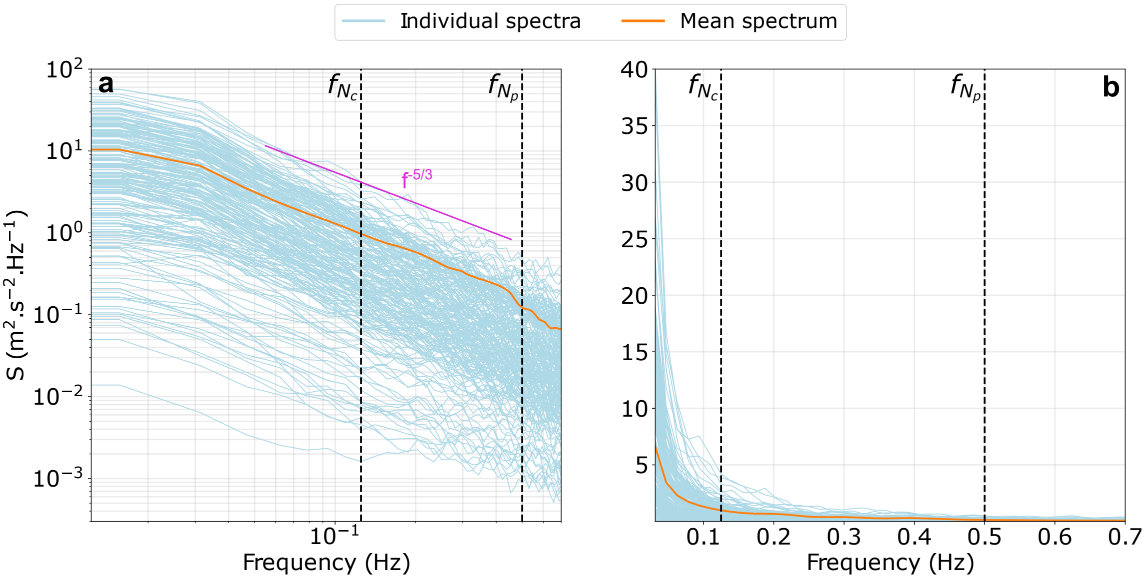

Figure 6. Individual spectra (light blue curves) and mean spectrum (orange curve) measured by the sonic anemometer over the 47-day measurement campaign, presented in log-log (a) and linear (b) formats. Vertical black dashed lines indicate the Nyquist frequencies, f_{N_c} and f_{N_p}, for the commercial and prototype lidar configurations respectively. The pink solid line in panel (a) shows the classic spectral slope $f^{-5/3}$.

minimize errors relative to the measured spectra. Fig. 7a illustrates an example of the three weighting scheme applied to a measured spectrum. This iterative process was conducted across both lidar configurations, yielding consistent results described hereafter.

The fitted spectra closely matched in the low-frequency domain, approximately up to f = 0.1 Hz, but strong divergences were observed thereafter. The low frequencies weighted scheme produced a curve substantially below the measured spectra at higher frequencies, whereas the unweighted scheme yielded a curve slightly above the measured spectra in this frequency range. In contrast, the high frequencies weighted scheme provided a fit that closely matched the measured spectra across all frequencies and exhibited the lowest mean error. For instance, when applied to the prototype lidar, the mean variance was 0.2321 m^2/s^2 for all integrated fitted spectra using the high-frequency weighted scheme, compared to 0.2262 m^2/s^2 for all integrated measured spectra. This results in an absolute error of 2.6%. Conversely, not employing any weighting during the fitting process resulted in an absolute error between the mean variance nearly three times higher, at 8.5%. Assigning weights to the low frequencies resulted in a mean absolute error exceeding six times that of the high-frequency weighted scheme, at 16.9%. Thus, the high-frequency weighted scheme was chosen for the fitting. An example of this fitting applied to individual LOS velocity spectra for both the commercial and prototype configurations is shown in Fig. 7b. This weighted scheme enabled the systematic identification of the plateau at higher frequencies, characteristic of white noise. Other weighting schemes did not consistently exhibit this plateau, making it challenging to reliably determine the value of N_i.

3.4 Instrumental noise

3.4.1 Comparison of the spectral and ACF methods

The spectral method yields a median variance that is 1.5 times higher than that of the ACF method for the commercial lidar and twice as high for the prototype lidar (Table 3). While this suggests differences in how each method characterizes noise, the spectral method also results in a mean instrumental noise that is 30-40% lower than that of the ACF method, indicating variations in the way noise is estimated. Moreover, the spread of mean values is notably narrower when using the spectral method, particularly for the commercial lidar, where it is reduced by half compared to the ACF method. This suggests a potential advantage in terms of consistency and stability. Given these observations, we used the spectral method to correct the measured variance, as it appeared to provide more stable estimates of instrumental noise.

3.4.2 Contribution of instrumental noise in the measured LOS velocity variances

This section evaluates, beam by beam, the impact of instrumental noise on the measured LOS velocity variances, which are combined to derive the along-wind variance (Eqs. 5-6). The parametric expression (Eq. 2) used to fit the LOS velocity spectra

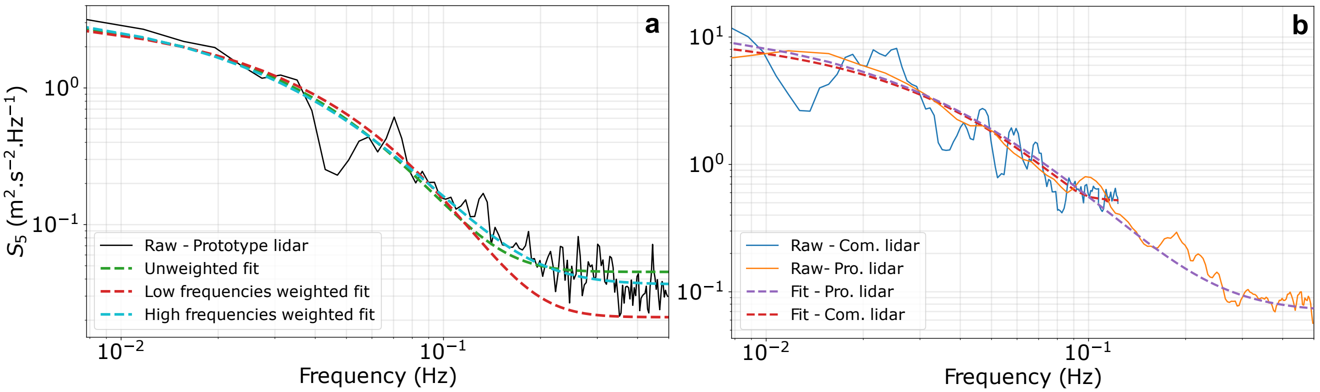

Figure 7. (a) Individual LOS velocity spectrum (solid black) of the prototype lidar fitted with Eq. 2 with three weighted schemes: unweighted fit (dashed green), low frequencies weighted fit (dashed red), and high frequencies weighted fit (dashed blue). (b) Individual LOS velocity spectrum measured by the commercial lidar (blue curve) and prototype lidar (orange curve) fitted with the high frequencies weighted scheme.

Table 3. Median and mean (± spread) variance of instrumental noise for commercial and prototype lidars, computed from the LOS velocity measurements across all beams using spectral and ACF methods.

	Commercial lidar		Prototype lidar	
Methods	Spectral	ACF	Spectral	ACF
Median (m^2/s^2)	0.0076	0.0050	0.0129	0.0081
Mean ± spread (m^2/s^2)	0.0108 ± 0.0102	0.0148 ± 0.0228	0.0181 ± 0.0175	0.0237 ± 0.0294

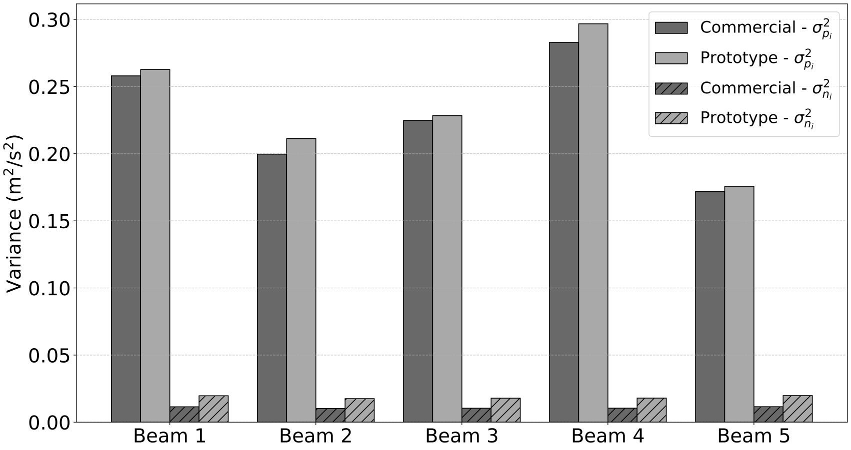

Figure 8. Mean variance of the net contribution from atmospheric turbulence ($\sigma^2_{p_i}$), corrected for instrumental noise derived from the spectral method, measured by each beam i at scales observable by the commercial (dark gray) and prototype (light gray) lidar profilers. Dashed areas represent the mean variance of instrumental noise, $\sigma^2_{n_i}$. The averages were computed over the 47-day dataset.

Table 4. Error Statistics of the along-wind standard deviation derived from the variance method, corrected for instrumental noise, applied on measurements collected by the commercial and prototype lidars in comparison to the reference sonic anemometer.

	Bias (m/s)	MAE (m/s)	RMSE (m/s)	R^2	Relative Error (%)
Commercial lidar	-0.0639	0.0886	0.1218	0.9138	7.8
Prototype lidar	-0.0466	0.0678	0.0871	0.9574	5.7

measured by beam i enables the identification of the power spectral density of instrumental noise, N_i, and the derivation of the variances, $\sigma^2_{n_i}$ (Eq. 4). Fig. 8 compares the mean magnitude of $\sigma^2_{n_i}$ to the mean variance of the net contribution from atmospheric turbulence, $\sigma^2_{p_i}$, corrected for instrumental noise at scales observable by the commercial and prototype lidar profilers.

The mean values of $\sigma^2_{n_i}$, which are nearly identical across all beams, were found to be 0.0108 m^2/s^2 for the commercial configuration (Table 3). A similar trend was observed for the prototype configuration, although the mean variance of instrumental noise was 68% higher, at 0.0181 m^2/s^2 (Table 3). Notably, the contribution of instrumental noise variance to the total variance, $\sigma^2_{b_i}$ (Eq. 3), was found to be 4.8% and 7.4% for the commercial and prototype lidar configurations, respectively.

The mean variances, $\sigma^2_{p_i}$ were consistently higher for measurements obtained with the prototype configuration. Across all beams, the mean value was 0.2288 m^2/s^2, which is 7.8% higher than the corresponding mean value for the commercial lidar measurements.

3.5 Along-wind standard deviation

Fig. 9 presents scatter plots of the along-wind standard deviation, $\hat{\sigma}$, derived from the variance method applied on measurements of both lidar configurations compared to the standard deviation, σ, obtained from the reference sonic anemometer. The prototype configuration demonstrates superior performance across all error metrics, with bias, MAE, and RMSE approximately 25% lower than those of the commercial configuration (Table 4). Additionally, the coefficient of determination is 5% higher. There is also a reduction in the relative error of the mean standard deviation, with the prototype configuration showing values of 5.7% compared to 7.8% for the commercial configuration.

Fig. 10 presents bin-averaged estimates of $\hat{\sigma}$ compared to estimates of σ (black curve) as a function of binned-averaged wind speed. For all wind speeds, the standard deviation measured by the sonic anemometer consistently remains higher than that derived from both lidar configurations. Below wind speed of 8 m/s, the standard deviation values from both lidar configurations closely match each other. Within this wind speed range, the standard deviation associated with the commercial lidar is 2.7% higher than that from the prototype configuration. However, above this wind speed threshold, the standard deviation associated with the prototype configuration increases more rapidly with wind speed compared to the commercial lidar. In this wind speed range, the standard deviation associated with the prototype lidar is 13.0% higher than that associated with the commercial configuration. For all wind speed ranges, the prototype lidar measurements exhibited a mean standard deviation and variance that were 2.9% and 7.2% higher, respectively, than those of the commercial configuration.

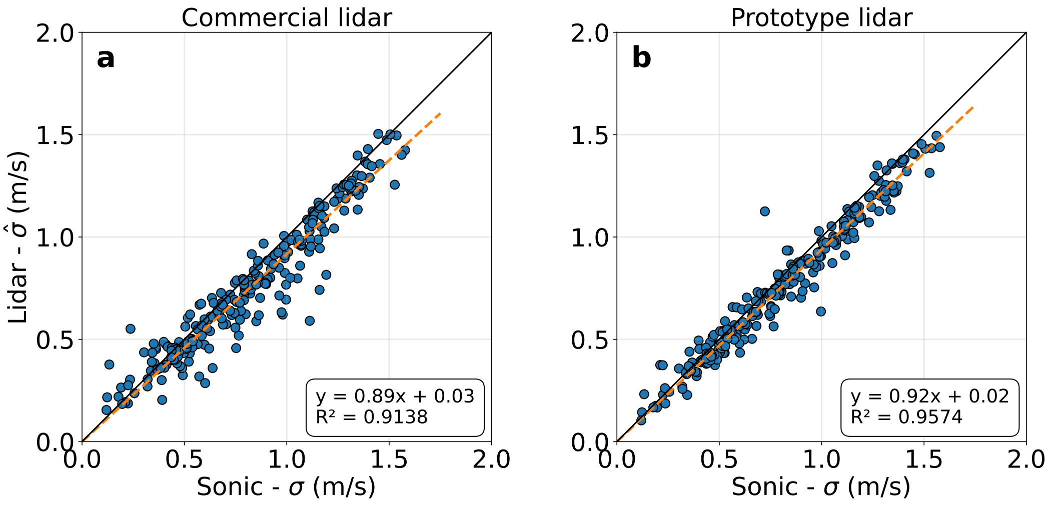

Figure 9. Scatter plots of along-wind standard deviation, $\hat{\sigma}$, derived from the variance method applied on measurements of the commercial and prototype lidar configurations versus standard deviation, σ, derived from the reference sonic anemometer. The standard deviation estimates are restricted to cases where wind direction was aligned with one pair of opposite beams.

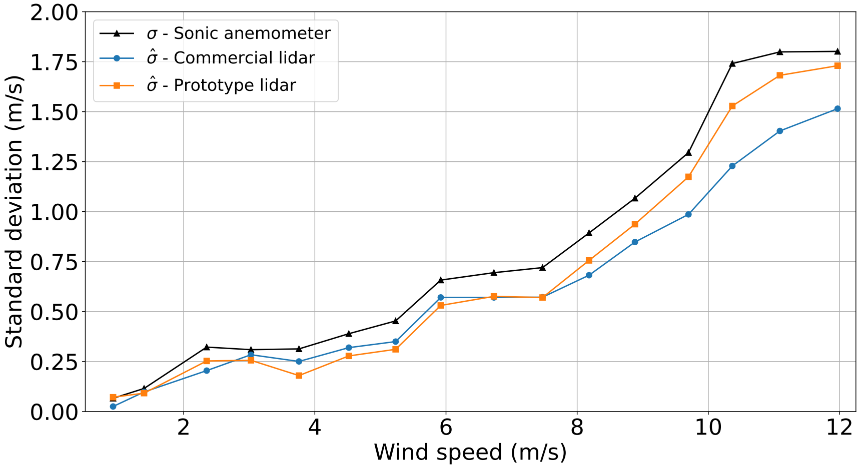

Figure 10. Along-wind standard deviation, $\hat{\sigma}$, derived from measurements of the commercial lidar (blue curve) and prototype lidar (orange curve), compared to the standard deviation, σ, obtained from reference sonic anemometer measurements (black curve) as a function of wind speed.

4 Discussion

When proposing an increase in sampling rate to capture smaller eddies and their associated energy through variance, it is essential to assess the instrumental noise and its variance to ensure that the observed changes are due to physical phenomena rather than noise. In this study, we estimate noise-induced variance using two distinct methods. For both lidar configurations, the mean variances of instrumental noise computed from two methods were found to be consistent with values obtained in previous studies, such as the WindCube lidar analysis by Mann et al. (2009). This alignment reinforces confidence in our estimates.

The increased sampling rate leads to higher instrumental noise compared to the commercial configuration, as expected, since the noise variance is inversely proportional to the number of transmitted pulses (Pearson et al., 2009). In the prototype lidar, achieving a higher sampling rate required reducing the number of pulses leading to the elevated noise levels. The noise variance was approximately 5% of the total variance for the commercial configuration and over 7% for the prototype configuration. While the noise contribution is relatively low, it is not negligible, and its impact should be considered when calculating second-order statistics of LOS velocities in pulsed wind lidar profilers.

Compared to estimates derived from the commercial lidar configuration, the error metrics (bias, MAE, RMSE) of the along-wind standard deviation estimates corrected for instrumental noise using the prototype lidar were notably lower. Additionally, the mean along-wind variance measured by the prototype was higher, suggesting that the increased sampling rate allows for improved detection of turbulent energy associated with smaller eddies. However, this observed improvement remains significantly below the theoretical benefit expected from increasing the LOS sampling rate, as determined through sonic anemometer measurements. The measurement volume of a sonic anemometer is effectively point-like, in comparison to the much larger probe length of wind lidar profilers. The anemometer is in fact essentially free of the intra-beam effect, which enables it to capture the wind signature of very small eddies.

One way to mitigate the impact of the intra-beam effect is by significantly reducing the probe length. A shorter probe length would minimize spatial averaging, enhancing the resolution of high-frequency fluctuations in the wind field. However, this reduction is likely to weaken the lidar echo strength, potentially increasing measurement errors. Therefore, a balance must be struck between improving resolution and maintaining signal quality.

The increased sampling rate of the prototype configuration could positively impact metrics such as turbulence intensity (TI), which is a key factor due to its influence on structural loads and turbine lifespan. As demonstrated in Fig. 10, this effect is expected to be more pronounced at higher wind speeds, such as at 15 m/s. At this wind speed, TI - referred to as TI15 - is used in design turbulence calculations to define characteristic standard deviation bands, which are essential for classifying turbines according to wind turbulence, as outlined in IEC 61400-1.

Moreover, the increased sampling rate extends the LOS velocity spectra over the frequency domain. This is particularly valuable for floating lidar systems, where measurements are used to derive TI through motion-compensation algorithms which is an ongoing research topic (e.g., Kelberlau et al., 2020; Désert et al., 2021). The buoy's motion generates energy spikes in the LOS velocity spectra at frequencies corresponding to the wave periods, the buoy's natural period, and their interactions (Thiébaut et al., 2024a). This introduces additional variance, $\sigma^2_{m_i}$, which must be accounted for alongside the three other variance terms that contribute to the total variance, $\sigma^2_{b_i}$, measured by each beam i (Eq. 3). With a Nyquist frequency of f_{N_c} = 0.125 Hz, the commercial configuration can detect motion-induced variance for periods up to 8 seconds, while lower-period motion remains undetectable. In contrast, the prototype configuration presented in this paper, with a Nyquist frequency of f_{N_p} = 0.5 Hz, enables the detection of motion effects for periods as short as 2 seconds. Thus, the prototype configuration may offer an advantage in developing motion-compensation algorithms based on the variance method by improving the derivation of true variance through LOS velocity spectra analysis.

The increased sampling rate resulted in a relatively slight 0.5% reduction in data availability compared to the commercial configuration over the 47-day dataset. While this difference is minimal, it may become more noticeable over longer measurement campaigns, which typically last over a year for wind site characterization. Following the measurement campaign presented in this paper, the prototype configuration was installed in December 2022 on Planier Island in the Mediterranean Sea, where it remains operational. The wind characteristics derived from the full year of 2023 are presented in Thiébaut et al. (2024b), including a detailed analysis of data availability. Encouragingly, up to 160 m above sea level, annual data availability exceeded the 90% threshold considered best practice. Beyond this height, availability gradually declined, reaching below 70% at 220 m. While this highlights an area for further optimization, the prototype lidar has already demonstrated strong performance at critical measurement heights.

Moreover, the prototype configuration performed comparably to the commercial setup in terms of mean wind characteristics. While the commercial configuration met the "best practice" threshold for all key performance indicators (KPIs), the prototype also achieved this standard, with the exception of mean wind speed differences, where it met the "minimum acceptance" level within the best practice range. This result is promising, as it confirms that the prototype lidar meets industry standards while offering opportunities for further refinement. With continued development, the prototype lidar has the potential to further enhance wind resource assessments and support the needs of modern wind energy projects.

5 Conclusions

This study highlights both the potential and challenges of enhancing the sampling rate in wind lidar systems, particularly for turbulence measurements and the detection of energy from smaller eddies. The prototype lidar configuration, with its increased sampling rate, demonstrated advantages in capturing higher-frequency fluctuations in the wind field, leading to more accurate along-wind variance estimates. By resolving smaller eddies, the prototype effectively captured additional turbulent energy that the commercial configuration, with its lower sampling rate, could not detect. This improvement was especially pronounced at higher wind speeds, where the prototype's reduced minimum detectable eddy size provided significant benefits. However, the theoretical gains expected from the increased sampling rate were not fully realized due to inherent measurement limitations within the probe, where spatial and temporal filtering effects constrain turbulence detection at certain scales.

The increased sampling rate also introduced some trade-offs, including elevated instrumental noise and a slight reduction in data availability. Noise contributions to the total variances were non-negligible and required correction to ensure accurate turbulence statistics. It is worth noting that a configuration similar to the prototype examined in this study could be achieved with a commercial lidar, as manufacturers can program an increased sampling rate with relative ease. However, users should be aware that implementing such a modification would require validation against a meteorological mast to obtain certification, which could add time and cost to deployment.

Another key consideration is balancing increased sampling rate with reduced probe length. Ideally, combining both enhancements would yield the optimal configuration, improving both temporal and spatial resolution. In this study, the increased sampling rate proved beneficial for turbulence measurements while maintaining acceptable accuracy for mean wind statistics. Meanwhile, the effects of reducing the probe length are currently under investigation. While further research is needed to determine its feasibility in field applications, this approach holds promise for future advancements in wind lidar profiler performance.

Author contributions

MT identified the problematic, performed the analysis and drafted the paper. FD and FG reviewed the manuscript.

Data and code availability

The data is owned by a private consortium with proprietary rights and confidentiality obligations, precluding its sharing alongside this paper.

Acknowledgments

We would like to acknowledge the team at Vaisala, including Mathias Régnier, Loïc Mahe and Cristina Benzo, for their support in providing and configuring the prototype lidar. We are deeply grateful to Louis Marié (Ifremer) for his valuable insights, which significantly contributed to improving the quality of this work.

Competing interest

The authors declare that they have no conflict of interest.

Financial support

This work was made possible through the support of France Energies Marines and the French government, managed by the Agence Nationale de la Recherche under the Investissements d'Avenir program, with the reference ANR-10-IEED-0006-34. This work was carried out in the framework of the POWSEIDOM project.

References

Bodini, N., Lundquist, J. K., and Newsom, R. K.: Estimation of turbulence dissipation rate and its variability from sonic anemometer and wind Doppler lidar during the XPIA field campaign, Atmospheric Measurement Techniques, 11, 4291–4308, 2018.

Bodini, N., Lundquist, J. K., Krishnamurthy, R., Pekour, M., Berg, L. K., and Choukulkar, A.: Spatial and temporal variability of turbulence dissipation rate in complex terrain, Atmospheric Chemistry and Physics, 19, 4367–4382, 2019.

Branlard, E., Pedersen, A. T., Mann, J., Angelou, N., Fischer, A., Mikkelsen, T., Harris, M., Slinger, C., and Montes, B. F.: Retrieving wind statistics from average spectrum of continuous-wave lidar, Atmospheric Measurement Techniques, 6, 1673–1683, 2013.

Browning, K. A. and Wexler, R.: The determination of kinematic properties of a wind field using Doppler radar, Journal of Applied meteorology and climatology, 7, 105–113, 1968.

Brugger, P., Träumner, K., and Jung, C.: Evaluation of a procedure to correct spatial averaging in turbulence statistics from a Doppler lidar by comparing time series with an ultrasonic anemometer, Journal of Atmospheric and Oceanic Technology, 33, 2135–2144, 2016.

Doviak, R. J. and Zrnic, D. S.: Doppler Radar & Weather Observations, Courier Corporation, Courier Corporation, 1993.

Durgesh, V., Thomson, J., Richmond, M. C., and Polagye, B. L.: Noise correction of turbulent spectra obtained from acoustic doppler velocimeters, Flow Measurement and Instrumentation, 37, 29–41, 2014.

Désert, T., Knapp, G., and Aubrun, S.: Quantification and correction of wave-induced turbulence intensity bias for a floating lidar system, Remote Sensing, 13, 2973, 2021.

Eberhard, W. L., Cupp, R. E., and Healy, K. R.: Doppler lidar measurement of profiles of turbulence and momentum flux, Journal of Atmospheric and Oceanic Technology, 6, 809–819, 1989.

Gal-Chen, T., Xu, M., and Eberhard, W. L.: Estimations of atmospheric boundary layer fluxes and other turbulence parameters from Doppler lidar data, Journal of Geophysical Research: Atmospheres, 97, 18 409–18 423, 1992.

Gargett, A. E., Tejada-Martinez, A. E., and Grosch, C. E.: Measuring turbulent large-eddy structures with an ADCP. Part 2. Horizontal velocity variance, 2009.

Guerra, M. and Thomson, J.: Turbulence Measurements from Five-Beam Acoustic Doppler Current Profilers, Journal of Atmospheric and Oceanic Technology, 34, 1267–1284, 2017.

Kelberlau, F. and Mann, J.: Cross-contamination effect on turbulence spectra from Doppler beam swinging wind lidar, Wind Energy Science, 5, 519–541, 2020.

Kelberlau, F., Neshaug, V., Lønseth, L., Bracchi, T., and Mann, J.: Taking the motion out of floating lidar: Turbulence intensity estimates with a continuous-wave wind lidar, Remote Sensing, 12, 898, 2020.

Kristensen, L., Kirkegaard, P., and Mikkelsen, T.: Determining the velocity fine structure by a laser anemometer with fixed orientation, Danmarks Tekniske Universitet, Risø Nationallaboratoriet for Bæredygtig Energi, 2011.

Kropfli, R. A.: Single Doppler radar measurements of turbulence profiles in the convective boundary layer, Journal of Atmospheric and Oceanic Technology, 3, 305–314, 1986.

Lenschow, D. H., Mann, J., and Kristensen, L.: How long is long enough when measuring fluxes and other turbulence statistics?, Journal of Atmospheric and Oceanic Technology, 11, 661–673, 1994.

Lenschow, D. H., Wulfmeyer, V., and Senff, C.: Measuring second-through fourth-order moments in noisy data, Journal of Atmospheric and Oceanic technology, 17, 1330–1347, 2000.

Lhermitte, R. M.: Note on wind variability with Doppler radar, Journal of Atmospheric Sciences, 19, 343–346, 1962.

Lhermitte, R. M.: Note on the observation of small-scale atmospheric turbulence by Doppler radar techniques, Radio Science, 4, 1241–1246, 1969.

Lu, Y. and Lueck, R. G.: Using a broadband ADCP in a tidal channel. Part II: Turbulence, Journal of Atmospheric and Oceanic Technology, 16, 1568–1579, 1999.

Mann, J., Cariou, J.-P., Courtney, M. S., Parmentier, R., Mikkelsen, T., Wagner, R., Lindelow, P., Sjoholm, M., and Enevoldsen, K.: Comparison of 3D turbulence measurements using three staring wind lidars and a sonic anemometer, Meteorologische Zeitschrift, 18, 135, 2009.

Mann, J., Peña, A., Bingöl, F., Wagner, R., and Courtney, M. S.: Lidar scanning of momentum flux in and above the atmospheric surface layer, Journal of Atmospheric and Oceanic Technology, 27, 959–976, 2010.

McMillan, J. M. and Hay, A. E.: Spectral and structure function estimates of turbulence dissipation rates in a high-flow tidal channel using broadband ADCPs, Journal of Atmospheric and Oceanic Technology, 34, 5–20, 2017.

Newman, J. F., Klein, P. M., Wharton, S., Sathe, A., Bonin, T. A., Chilson, P. B., and Muschinski, A.: Evaluation of three lidar scanning strategies for turbulence measurements, Atmospheric Measurement Techniques, 9, 1993–2013, 2016.

Olesen, H. R., Larsen, S. E., and Højstrup, J.: Modelling velocity spectra in the lower part of the planetary boundary layer, Boundary-Layer Meteorology, 29, 285–312, 1984.

O'Connor, E. J., Illingworth, A. J., Brooks, I. M., Westbrook, C. D., Hogan, R. J., Davies, F., and Brooks, B. J.: A method for estimating the turbulent kinetic energy dissipation rate from a vertically pointing Doppler lidar, and independent evaluation from balloon-borne in situ measurements, Journal of atmospheric and oceanic technology, 27, 1652–1664, 2010.

Pearson, G., Davies, F., and Collier, C.: An analysis of the performance of the UFAM pulsed Doppler lidar for observing the boundary layer, Journal of Atmospheric and Oceanic Technology, 26, 240–250, 2009.

Peña, A., Hasager, C. B., Gryning, S., Courtney, M., Antoniou, I., and Mikkelsen, T.: Offshore wind profiling using light detection and ranging measurements, Wind Energy, 12, 105–124, 2009.

Richard, J.-B., Thomson, J., Polagye, B., and Bard, J.: Method for identification of doppler noise levels in turbulent flow measurements dedicated to tidal energy, International Journal of Marine Energy, 3, 52–64, 2013.

Rippeth, T. P., Williams, E., and Simpson, J. H.: Reynolds stress and turbulent energy production in a tidal channel, Journal of Physical Oceanography, 32, 1242–1251, 2002.

Sathe, A. and Mann, J.: Measurement of turbulence spectra using scanning pulsed wind lidars, Journal of Geophysical Research: Atmospheres, 117, 2012.

Sathe, A., Mann, J., Gottschall, J., and Courtney, M. S.: Can wind lidars measure turbulence?, Journal of Atmospheric and Oceanic Technology, 28, 853–868, 2011.

Sjöholm, M., Mikkelsen, T., Mann, J., Enevoldsen, K., and Courtney, M.: Spatial averaging-effects on turbulence measured by a continuous-wave coherent lidar, Meteorologische Zeitschrift (Berlin), 18, 2009.

Smalikho, I., Köpp, F., and Rahm, S.: Measurement of atmospheric turbulence by 2-μ m Doppler lidar, Journal of Atmospheric and Oceanic Technology, 22, 1733–1747, 2005.

Stacey, M. T., Monismith, S. G., and Burau, J. R.: Measurements of Reynolds stress profiles in unstratified tidal flow, Journal of Geophysical Research, 104, 10 935–10 949, 1999a.

Stacey, M. T., Monismith, S. G., and Burau, J. R.: Observations of turbulence in a partially stratified estuary, Journal of Physical Oceanography, 29, 1950–1970, publisher: American Meteorological Society, 1999b.

Strauch, R. G., Merritt, D. A., Moran, K. P., Earnshaw, K. B., and De Kamp, D. V.: The Colorado wind-profiling network, Journal of Atmospheric and Oceanic Technology, 1, 37–49, 1984.

Stull, R. B.: Meteorology for scientists and engineers: a technical companion book with Ahrens' Meteorology Today, 2000.

Teunissen, H. W.: Structure of mean winds and turbulence in the planetary boundary layer over rural terrain, Boundary-Layer Meteorology, 19, 187–221, 1980.

Theriault, K.: Incoherent multibeam Doppler current profiler performance: Part II–Spatial response, IEEE journal of oceanic engineering, 11, 16–25, 1986.

Thiébaut, M., Filipot, J.-F., Maisondieu, C., Damblans, G., Duarte, R., Droniou, E., Chaplain, N., and Guillou, S.: A comprehensive assessment of turbulence at a tidal-stream energy site influenced by wind-generated ocean waves, Energy, 191, 116 550, 2020.

Thiébaut, M., Quillien, N., Maison, A., Gaborieau, H., Ruiz, N., MacKenzie, S., Connor, G., and Filipot, J.-F.: Investigating the flow dynamics and turbulence at a tidal-stream energy site in a highly energetic estuary, Renewable Energy, 195, 252–262, 2022.

Thiébaut, M., Thebault, N., Le Boulluec, M., Damblans, G., Maisondieu, C., Benzo, C., and Guinot, F.: Experimental Evaluation of the Motion-Induced Effects for Turbulent Fluctuations Measurement on Floating Lidar Systems, Remote Sensing, 16, 1337, 2024a.

Thiébaut, M., Vonta, L., Benzo, C., and Guinot, F.: Characterization of the offshore wind dynamics for wind energy production in the Gulf of Lion, Western Mediterranean Sea, Wind Energy and Engineering Research, 1, 100 002, 2024b.

Thomson, J., Polagye, B., Durgesh, V., and Richmond, M. C.: Measurements of turbulence at two tidal energy sites in Puget Sound, WA, Oceanic Engineering, IEEE Journal of Oceanic Engineering, 37, 363–374, 2012.

Tieleman, H. W.: Universality of velocity spectra, Journal of Wind Engineering and Industrial Aerodynamics, 56, 55–69, 1995.

Welch, P.: The use of fast Fourier transform for the estimation of power spectra: A method based on time averaging over short, modified periodograms, IEEE Transactions on audio and electroacoustics, 15, 70–73, 1967.

Wildmann, N., Bodini, N., Lundquist, J. K., Bariteau, L., and Wagner, J.: Estimation of turbulence dissipation rate from Doppler wind lidars and in situ instrumentation for the Perdigão 2017 campaign, Atmospheric Measurement Techniques, 12, 6401–6423, 2019.

Wilson, D. A.: Doppler radar studies of boundary layer wind profile and turbulence in snow conditions, 1970.